Phase transition of layer-stacked borophene under pressure

Xiao-Ji Weng,[1,2] QuanSheng Wu,[3,4] Xi Shao,[2] Oleg V. Yazyev,[3,4] Xin-Ling He,[1] Xiao Dong,[1] Hui-Tian Wang,[5] Xiang-Feng Zhou,[1,2,*] and Yongjun Tian[2]

[1]*Key Laboratory of Weak-Light Nonlinear Photonics and School of Physics, Nankai University, Tianjin 300071, China*

[2]*State Key Laboratory of Metastable Materials Science and Technology, School of Science, Center for High Pressure Science, Yanshan University, Qinhuangdao 066004, China*

[3]*Institute of Physics, École Polytechnique Fédérale de Lausanne (EPFL), CH-1015 Lausanne, Switzerland*

[4]*National Centre for Computational Design and Discovery of Novel Materials MARVEL, Ecole Polytechnique Fédérale de Lausanne (EPFL), CH-1015 Lausanne, Switzerland*

[5]*National Laboratory of Solid State Microstructures and Collaborative Innovation Center of Advanced Microstructures, Nanjing University, Nanjing 210093, China*

(Received 29 October 2021; revised 6 March 2022; accepted 27 May 2022; published 8 June 2022)

The 8-*Pmmn* borophene, a boron analog of graphene, hosts tilted and anisotropic massless Dirac fermion quasiparticles owing to the presence of a distorted graphenelike sublattice. First-principles calculations show that stacked 8-*Pmmn* borophene is transformed into fused three-dimensional borophene under pressure, being accompanied by partial bond breaking and bond reformation. Strikingly, fused 8-*Pmmn* borophene inherits the Dirac band dispersion resulting in an unusual semimetal-semimetal transition. A simple tight-binding model derived from graphene qualitatively reveals the underlying physics due to the maximum preservation of the graphenelike substructure after the phase transition, which contrasts greatly to the transformation of graphite into diamond associated with the semimetal-insulator transition.

DOI: 10.1103/PhysRevB.105.235410

I. INTRODUCTION

Graphene, a monolayer material exfoliated from graphite, has attracted immense interest partially owing to its remarkable thermal stability, superior mechanical strength, and unique Dirac-semimetallic band structure [1–3]. Graphene shows a significant potential for applications in the fields of electronics, batteries, sensors, structural materials, and more. Boron, the element that neighbors carbon in the second row of the periodic table and forms a nonmetallic solid, has also been proved to own its two-dimensional (2D) form, termed borophene [4–6]. Borophene shares much in common with graphene, but has its own uniqueness due to complex multicenter bonds. Both theoretical simulations and experiments extensively explored the diverse geometrical configurations (i.e., planar, quasiplanar, or multilayer structures) and versatile properties (i.e., superconductivity, magnetism, or negative Poisson's ratio) in various borophenes [4–11]. For instance, 8-*Pmmn* borophene, featured by an 8-atom orthorhombic unit cell with *Pmmn* symmetry [9], is composed of a distorted graphenelike boron sheet and attached boron chains. As shown in Fig. 1, the boron chains are attached above and below the distorted graphenelike sheet. Each B-B pair along the chain direction donates two electrons to the distorted hexagonal lattice, satisfying the isoelectronic state of graphene and resulting in a tilted and anisotropic Dirac cone at the Fermi level (E_F). The maximum Fermi velocity of 8-*Pmmn* borophene along the chain direction is nearly 1.5 times that of graphene [9]. Such a unique band structure stimulated further study of the electronic properties of 8-*Pmmn* borophene, such as anisotropic plasmons, magnetotransport properties, anomalous Klein tunneling, valley-dependent electron retroreflection, Veselago focusing, Ruderman-Kittel-Kasuya-Yosida exchange interaction, metal-insulator transition, and the photoinduced Hall effect [12–21]. Most recently, a variety of exotic electronic states, including flat-band phases, superconductivity, magnetism, and the Chern insulator phases, were discovered moiré superlattice systems based on multilayer graphene [22–26]. These new discoveries made a very strong impact in condensed matter physics and beyond. Therefore, it is important to investigate the bulk stacked borophenes as well as their interesting nodal-line semimetallic properties [27–31].

II. METHOD

In this paper, boron polymorphs derived from 8-*Pmmn* borophene have been studied using the projector augmented-wave (PAW) method as implemented in the VASP code [32,33]. The exchange correlation energy was treated within the generalized gradient approximation (GGA) using the functional of Perdew, Burke, and Ernzerhof (PBE) [34]. The plane-wave energy cutoff of 500 eV, energy convergence criterion of 10^{-7} eV, force criterion of 0.003 eV/Å, and k-point resolution of $2\pi \times 0.04$ Å^{-1} were employed for the density functional theory (DFT) calculation, which showed excellent convergence of the total energy, stress tensors, and lattice parameters. To examine the energetic and dynamical stability, the semiempirical dispersion-correction method (DFT-D3) was applied

*xfzhou@nankai.edu.cn; zxf888@163.com

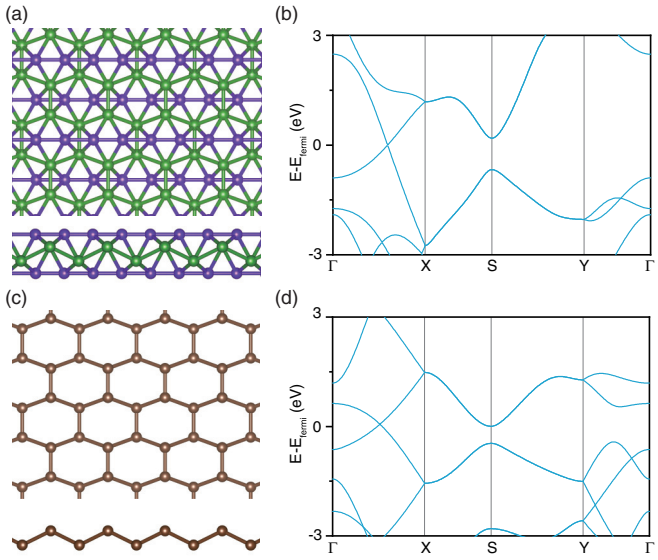

FIG. 1. (a) and (b) The crystal structure and band structure of 8-*Pmmn* borophene. The distorted graphenelike sublattice is colored in green while the attached boron chains are colored in purple. (c) and (d) The crystal structure and band structure of graphene with the same honeycomb lattice as 8-*Pmmn* borophene.

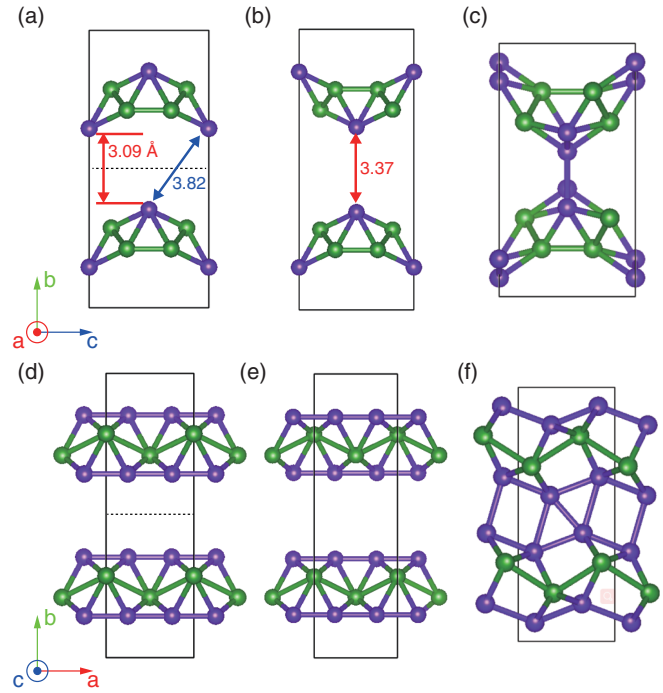

FIG. 2. (a)–(c) Projection along the [100] direction of AA-8-*Pmnm* ($1 \times 2 \times 1$ supercell), AB-16-*Amam* (conventional cell), and the fused AB-16-*Pnnm* phase. (d)–(f) Projection along the [001] direction of AA-8-*Pmnm*, AB-16-*Amam*, and the fused AB-16-*Pnnm* phases.

to the various boron allotropes [35]. A phonon spectrum was calculated by the PHONOPY code within the density functional perturbation theory (DFPT) framework [36]. Moreover, *ab initio* molecular dynamics (AIMD) simulations within the canonical ensemble (NVT) were performed using a $2 \times 2 \times 2$ supercell and a Nosé-Hoover thermostat [37].

III. RESULTS AND DISCUSSION

Two layer-stacked borophene configurations are constructed from the parent 8-*Pmmn* structure, and designated as AA-8-*Pmnm* and AB-16-*Amam* borophenes. Two sublattices of the 8-*Pmnm* borophene are illustrated in Fig. 2 using different colors. The AA-8-*Pmnm* configuration was constructed from 8-*Pmmn* borophene without introducing any lateral shift in the (010) plane, while there is a shift of half of the lattice parameter c in the AB-16-*Amam* phase. The lattice parameters

TABLE I. Structural parameters and the vdW-corrected total energies of the studied boron allotropes at zero pressure.

Structure (symmetry)	Lattice parameters (Å)	Atomic position (fractional coordinates)	Total energy (eV/atom)
AA-8-*Pmnm*	$a = 3.25, b = 5.27, c = 4.51$ $\alpha = \beta = \gamma = 90^\circ$	*B*1(0.000, 0.424, 0.184) *B*2(0.247, 0.707, 0.000)	−6.420
AB-16-*Amam*	$a = 3.25, b = 11.10, c = 4.51$ $\alpha = \beta = \gamma = 90^\circ$	*B*1(0.000, 0.152, 0.003) *B*2(0.184, 0.286, 0.250)	−6.415
AB-16-*Pnnm*	$a = 3.20, b = 8.48, c = 4.50$ $\alpha = \beta = \gamma = 90^\circ$	*B*1(0.171, 0.074, 0.000) *B*2(0.159, 0.352, 0.500) *B*3(0.136, 0.690, 0.188)	−6.519
α-B_{12} ($R\bar{3}m$)	$a = b = c = 5.03$ $\alpha = \beta = \gamma = 58.0^\circ$	*B*1(0.010, 0.010, 0.654) *B*2(0.222, 0.222, 0.630)	−6.808
8-*Pmmn* [9]	$a = 3.25, b = 4.52, c = 13.00$ $\alpha = \beta = \gamma = 90^\circ$	*B*1(0.000, 0.316, 0.531) *B*2(0.253, 0.000, 0.584)	−6.395
3D borophene [38] (*Immm*)	$a = 5.14, b = 1.85, c = 2.80$ $\alpha = \beta = \gamma = 90^\circ$	*B*1(0.167, 0.000, 0.000)	−6.429
3D-α' boron [39] (*Cmcm*)	$a = 7.82, b = 8.00, c = 5.05$ $\alpha = \beta = \gamma = 90^\circ$	*B*1(0.000, 0.398, 0.568) *B*2(0.168, 0.289, 0.084) *B*3(0.176, 0.304, 0.750)	−6.431
α sheet [40] (*P*6/*mmm*)	$a = b = 5.06, c = 15.00$ $\alpha = \beta = 90^\circ, \gamma = 120^\circ$	*B*1(0.000, 0.332, 0.500) *B*2(0.333, 0.667, 0.500)	−6.332

and atomic positions of the stacked borophenes compared with other related boron allotropes are listed in Table I. The lattice parameters a and c of AA-8-*Pmnm* and AB-16-*Amam* borophenes are almost the same as those of the 8-*Pmmn* structure. The B-B bond lengths of these two stacked borophenes are ranging from 1.61 to 1.91 Å. To investigate the interlayer distance of the stacked borophenes, the van der Waals (vdW) interaction has been considered. Owing to the quasiplanar structure, first-principles calculations show that interlayer distances (the height difference between the downmost atoms in the upper layer and the topmost atoms in the lower layer) are 3.09 and 3.37 Å for AA-8-*Pmnm* and AB-16-*Amam* borophenes, respectively. These distances are slightly shorter than the interlayer spacing in graphite, and the corresponding calculated value of 3.45 Å is in good agreement with the experimental value [41]. Hence, both the stacking sequence and the puckered structure of 8-*Pmmn* borophene result in a different interlayer distance. The AA-8-*Pmnm* structure is 5 meV/atom lower in energy than the AB-16-*Amam* structure. Note that the calculated energy difference between the bulk phases of α-B_{12} and β-B_{106} is about 2 meV/atom [42]. Therefore, the stacking sequence plays a decisive role in the relative stability of vdW-coupled stacked borophenes. Both the AA-8-*Pmnm* and AB-16-*Amam* borophene configurations are close in energy compared to other predicted three-dimensional (3D) boron phases (see Table I), but are higher in energy relative to bulk α-B_{12}, indicating these are metastable phases. While various structures of borophene have been reported, neither stacked nor fused borophenes have been explored extensively [38,43], and even less so for their high-pressure phases.

Graphite can be converted into a novel form of diamond (cold compressed graphite) at high pressure or cubic diamond at high pressure and high temperature as a result of the sp^2-sp^3 transition [Figs. 3(a)–3(c)] [44,45]. It is interesting to study the behavior of the stacked borophenes under pressure [Figs. 3(e) and 3(f)]. The calculated pressure-enthalpy curves of the stacked borophene configurations are presented in Fig. 3(g). One observes that the AA-8-*Pmnm* phase is thermodynamically more stable than the AB-16-*Amam* phase up to 2.75 GPa. Strikingly, the enthalpy of AB-16-*Amam* borophene decreases abruptly at 3 GPa, suggesting a structural phase transition. The variation of lattice parameter b as a function of pressure is shown in Fig. 3(h). This quantity also exhibits an abrupt decrease at the phase transition point for AB-16-*Amam* borophene. By analyzing the relaxed structure of the AB-16-*Amam* phase at 3 GPa, we conclude that the phase transition takes place by overcoming the weak vdW interaction with bond breaking and bond reforming, leading to the connection of the adjacent layers. The relaxed structure is referred to as fused AB-16-*Pnnm* borophene [Figs. 2(c) and 2(f)]. Compared to the AB-16-*Amam* structure, the graphene-like sublattice in fused AB-16-*Pnnm* borophene is retained, while the boron chains in the adjacent layers are connected in a puckered arrangement. Although the interlayer distance in the AA-8-*Pmnm* phase (3.09 Å) is shorter than that in the AB-16-*Amam* phase (3.37 Å), as shown in Figs. 2(a) and 2(b), the nearest B-B distance between the adjacent layers in the AA-8-*Pmnm* phase (3.82 Å) is longer than its interlayer distance (3.09 Å), whereas it is the same for AB-16-*Amam* borophene (3.37 Å). The longer B-B distance between adjacent layers in AA-8-*Pmnm* borophene seems to prevent the occurrence of a direct phase transformation. Furthermore, the MD simulations showed the vdW-coupled borophenes were dynamically unstable and transformed to the fused phase under some conditions, whereas fused AB-16-*Pnnm* borophene was dynamically stable at least up to 1000 K. The dynamical stability of fused AB-16-*Pnnm* borophene was also confirmed by its phonon dispersion curve [46].

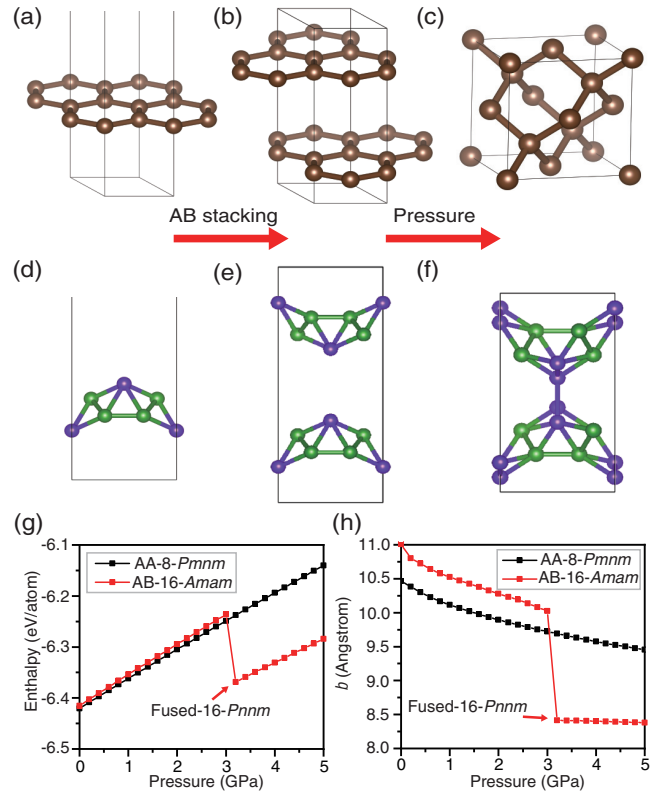

FIG. 3. The illustration for the phase transition of (a)–(c) graphite and (d)–(f) stacked borophene under pressure. (g) Enthalpy and (h) lattice parameter b of stacked borophene as a function of pressure.

The 8-*Pmmn* borophene hosts tilted and anisotropic massless Dirac fermion quasiparticles owing to its unique crystal structure. For the 2D 8-*Pmmn* phase, as the interlayer distance is larger than 10 Å (along the y direction), there is no interaction between adjacent layers. As the interlayer distance is decreased to a certain value (e.g., 3.37 Å), AB-16-*Amam* borophene is formed. The interlayer coupling transforms the Dirac points of 8-*Pmmn* borophene into the nodal lines of AB-16-*Amam* borophene [Figs. 4(a) and 4(b)]. As the interlayer distance is further decreased, AB-16-*Amam* borophene may transform into the fused AB-16-*Pnnm* phase under pressure (or under uniaxial compression). The mechanism underlying the band-structure evolution is complex but intriguing. As shown in Fig. 4(c), the orbital-resolved band structure shows that the fused AB-16-*Pnnm* borophene is a semimetal with several crossing points at the vicinity of the Fermi level E_F. Furthermore, the electrons at the crossing points 1 and 3 and the holes at the points 2 and 4 lead to nonzero density of states (DOS) at E_F. The densities of the electrons and holes

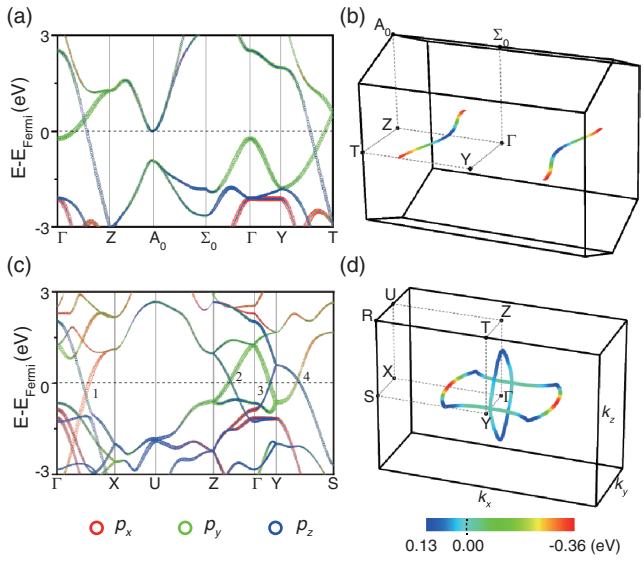

FIG. 4. (a), (c) Band structures of AB-16-*Amam* and fused AB-16-*Pnnm* borophene, respectively. Red, green, and blue colors indicate the weight of p_x, p_y, and p_z orbitals, respectively. (b), (d) The corresponding distribution of the crossing points for (a), (c).

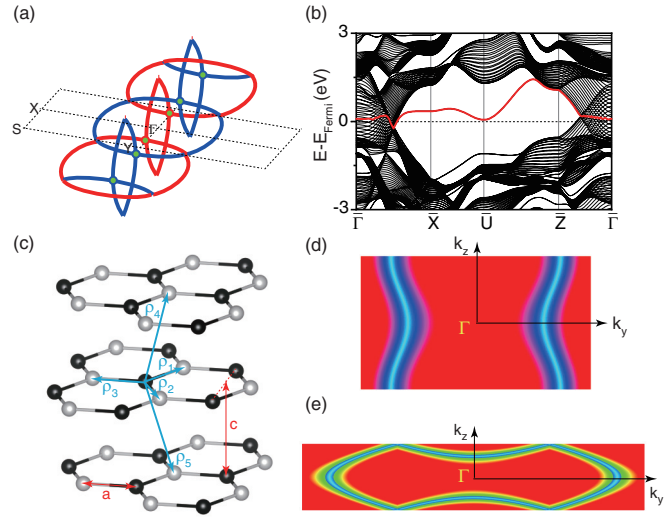

FIG. 5. (a) The distribution of the nodal lines of fused AB-16-*Pnnm* borophene in the extended Brillouin zone. Two sets of nodal chains are colored in red and blue. The touching nodal points are colored in green. (b) The (010) surface states of fused AB-16-*Pnnm* borophene. (c) The graphene model adopted the same stacking sequence as AB-16-*Amam* borophene while ignoring the buckling, and two inequivalent sites are colored in black and gray, respectively. (d) and (e) The nodal line described by Eq. (1) when $J' = -0.1J$ and $J' = -0.9J$. The BZ plotted in (d) and (e) represent the different symmetries of AB-16-*Amam* and fused AB-16-*Pnnm* borophenes.

are evaluated by integrating their occupations of four bands near E_F [42]. The calculated electron and hole concentrations are equal to 1.76×10^{20} cm^{-3}, which is less than the commonly accepted upper limit for semimetals (10^{22} cm^{-3}). The coexistence of twofold and fourfold degenerate crossing points associated with the same concentration of electrons and holes suggests that fused AB-16-*Pnnm* borophene is a compensated topological semimetal (TSM). For the crossing point 1 at the Γ-X segment, the Fermi velocities along the k_x direction are 1.04×10^6 and 1.10×10^6 m/s, exceeding the calculated value of graphene (0.82×10^6 m/s) and being almost the same as the maximum value for 8-*Pmmn* borophene (1.16×10^6 m/s) [9]. As a result, AB-16-*Pnnm* borophene partly inherits the Dirac band dispersion of the 8-*Pmmn* structure in the k_x direction, while the dispersion is different in the k_y-k_z plane. Further band-structure calculations show the nodal-line distribution of the fused AB-16-*Pnnm* phase in the extended Brillouin zone (BZ) [Figs. 4(d) and 5(a)], consisting of overlapping nodal loops in the k_x-k_y plane (by crossing the BZ boundary), while the nodal loops in the k_y-k_z plane are separated. These two sets of nodal lines are orthogonal and intersect at the crossing point 3 [Fig. 4(c)]. According to the space group *Pnnm*, the point groups on the ΓXSY and ΓYTZ planes are both C_s. The nodal loops in the k_x-k_y plane are protected by the mirror operator M_z, whereas others in the k_y-k_z plane are protected by the glide operator $\{M_z|\boldsymbol{a}/2 + \boldsymbol{b}/2 + \boldsymbol{c}/2\}$ [46]. Overall, fused AB-16-*Pnnm* borophene can be classified as a nodal-chain semimetal. One of the most interesting features of the nodal-line materials is the presence of drumhead surface states, which may provide a route to higher-temperature superconductivity [47,48]. The surface states of fused AB-16-*Pnnm* borophene are calculated using the 15-layer-thick (010) slab model. As shown in Fig. 5(b), the drumheadlike surface state (colored in red) connects nodal points 1 and 2 in the $\overline{\Gamma}$-$\overline{X}$-$\overline{U}$-$\overline{Z}$-$\overline{\Gamma}$ path. The dispersion is flat around the high-symmetry point $\overline{X}$, which is expected to facilitate detection in future experiments. We would like to point out that spin-orbit coupling (SOC) can break the symmetry and open a band gap at the crossing point. However, due to the very weak SOC in the studied light-element systems, only a tiny gap opens at the nodal points, e.g., ∼1.35 meV at the fourfold degenerate point, which is too weak to affect the semimetal properties.

Due to the buckling for the graphenelike substructure in 8-*Pmmn* borophene, the out-of-plane states are dominantly originating from the p_z orbitals while having a partial projection of p_x and p_y orbitals [9]. The out-of-plane states form two similar π bands as graphene (Fig. 1), which are the key factors for the Dirac band structure in 8-*Pmmn* borophene. Therefore, a two-band tight-binding (TB) model derived from graphene is constructed to qualitatively analyze the electronic evolution from the Dirac semimetal to nodal-line semimetal after stacking 8-*Pmmn* borophene to form 3D structures. As shown in Fig. 5(c), the nearest intralayer and interlayer hopping vectors from two inequivalent sites were considered as

$$\boldsymbol{\rho_1} = \frac{a}{2}\hat{x} + \frac{\sqrt{3}a}{2}\hat{y}, \quad \boldsymbol{\rho_2} = \frac{a}{2}\hat{x} - \frac{\sqrt{3}a}{2}\hat{y}, \quad \boldsymbol{\rho_3} = -a\hat{x},$$
$$\boldsymbol{\rho_4} = \frac{a}{2}\hat{x} + c\hat{z}, \quad \boldsymbol{\rho_5} = \frac{a}{2}\hat{x} - c\hat{z}.$$

The TB Hamiltonian based on the p_z orbital was constructed to reveal the band structure in proximity of the

E_F as

$$E(k) = \pm\Bigg[2J'^2[1+\cos(2ck_z)] + J^2\left\{3+2\cos(\sqrt{3}k_y a)+4\cos\left[\frac{3}{2}a\left(k_x-\frac{2\pi}{3a}\right)\right]\times\cos\left(\frac{3}{2}k_y a\right)\right\} + 4JJ'\cos(ck_z)\left\{2\cos\left(\frac{\sqrt{3}}{2}ak_y\right)+\cos\left[\frac{3}{2}a\left(k_x-\frac{2\pi}{3a}\right)\right]\right\}\Bigg]^{0.5}, \quad (1)$$

where the parameters of J, J', a, and c represent the intralayer hopping strength, interlayer hopping strength, C-C bond length, and interlayer distance, respectively. Assuming $J > 0$ and plotting the band structure at plane of $k_x = 0$, the electronic transition arose from the Dirac semimetal to nodal-line semimetal when $-0.5J < J' < 0$, which corresponds to stacking 8-*Pmmn* borophene into AB-16-*Amam* borophene [Figs. 4(b) and 5(d)]. Similarly, the electronic transition is transformed from a nodal-line semimetal to nodal-loop or nodal-chain semimetal when $J' < -0.5J$, for instance, the phase transition from AB-16-*Amam*-borophene to fused AB-16-*Pnnm* borophene [Figs. 4(d) and 5(e)]. Reducing the value of J' indicates the enhancement of the interlayer interaction. Note that the interlayer interaction of $J' < -0.5J$ is prohibited in the stacked graphene system. The interlayer interaction is too strong to break the graphene sheets, leading to the phase transition from graphite to diamond, while it can be realized in the stacked 8-*Pmmn* borophene system. As long as the graphenelike substructure is preserved, the essence of the topological semimetal is retained even if there is partial bond breaking and reformation during the phase transition [46].

IV. CONCLUSION

In conclusion, we investigated stacked 8-*Pmmn* borophene in different forms. Under increasing pressure, the interatomic distances typically decreased. The valence and conduction bands are thus expected to broaden, leading to pressure-induced metallization [49]. The AB-stacked borophene is transformed into fused borophene at ∼3 GPa associated with bond breaking and reformation between the adjacent boron chains. However, due to the preserved graphenelike substructure, the pressure-induced semimetal-semimetal transition takes place in stacked 8-*Pmmn* borophene—that is, a nodal-line semimetal (AB-16-*Amam* phase) transforms into a nodal-chain semimetal (fused AB-16-*Pnnm* phase), which is different from the common semimetal-metal (semimetal-semiconductor) transition. Recently, bilayer borophenes were successfully synthesized on Ag(111) and Cu(111) substrates [50,51]. Meanwhile, 8-*Pmmn* borophene was predicted to be grown on the metal substrates because its lattice constants match the (110) surface of several metals and metal oxides [9,52]. It is therefore anticipated that layer-stacked borophenes might be synthesized in the near future. If the synthesis succeeds, new bulk allotropes of boron could be formed under pressure and may be quenchable to ambient condition. These would extremely expand the phase diagram of elemental boron.

ACKNOWLEDGMENTS

This work was supported by the National Natural Science Foundation of China (Grants No. 52025026, No. 11874224, and No. 52090020). Q.W. and O.V.Y. acknowledge support from the NCCR Marvel. The calculation was performed on the TianheII supercomputer at Chinese National Supercomputer Center in Guangzhou and at the Swiss National Supercomputing Centre (CSCS) under Project No. s1008.

[1] K. S. Novoselov, A. K. Geim, S. V. Morozov, D. Jiang, Y. Zhang, S. V. Dubonos, I. V. Grigorieva, and A. A. Firsov, Science **306**, 666 (2004).
[2] K. S. Novoselov, A. K. Geim, S. V. Morozov, D. Jiang, M. I. Katsnelson, I. V. Grigorieva, S. V. Dubonos, and A. A. Firsov, Nature (London) **438**, 197 (2005).
[3] W. Choi, I. Lahiri, R. Seelaboyina, and Y. S. Kang, Crit. Rev. Solid State Mater. Sci. **35**, 52 (2010).
[4] Z. A. Piazza, H.-S. Hu, W.-L. Li, Y.-F. Zhao, J. Li, and L.-S. Wang, Nat. Commun. **5**, 3113 (2014).
[5] A. J. Mannix, X.-F. Zhou, B. Kiraly, J. D. Wood, D. Alducin, B. D. Myers, X. Liu, B. L. Fisher, U. Santiago, J. R. Guest, M. J. Yacaman, A. Ponce, A. R. Oganov, M. C. Hersam, and N. P. Guisinger, Science **350**, 1513 (2015).
[6] B. Feng, J. Zhang, Q. Zhong, W. Li, S. Li, H. Li, P. Cheng, S. Meng, L. Chen, and K. Wu, Nat. Chem. **8**, 563 (2016).
[7] E. S. Penev, A. Kutana, and B. I. Yakobson, Nano Lett. **16**, 2522 (2016).
[8] X.-F. Zhou, A. R. Oganov, Z. Wang, I. A. Popov, A. I. Boldyrev, and H.-T. Wang, Phys. Rev. B **93**, 085406 (2016).
[9] X.-F. Zhou, X. Dong, A. R. Oganov, Q. Zhu, Y. Tian, and H.-T. Wang, Phys. Rev. Lett. **112**, 085502 (2014).
[10] M. H. Zhu, X. J. Weng, G. Gao, S. Dong, L. F. Lin, W. H. Wang, Q. Zhu, A. R. Oganov, X. Dong, Y. Tian, X.-F. Zhou, and H. T. Wang, Phys. Rev. B **99**, 205412 (2019).
[11] J.-H. Yang, S. Song, S. Du, H.-J. Gao, and B. I. Yakobson, J. Phys. Chem. Lett. **8**, 4594 (2017).
[12] X. Zhou, Phys. Rev. B **102**, 045132 (2020).
[13] SK Firoz Islam and A. M. Jayannavar, Phys. Rev. B **96**, 235405 (2017).
[14] K. Sadhukhan and A. Agarwal, Phys. Rev. B **96**, 035410 (2017).
[15] SK Firoz Islam, J. Phys.: Condens. Matter **30**, 275301 (2018).
[16] S.-H. Zhang and W. Yang, Phys. Rev. B **97**, 235440 (2018).
[17] X. Zhou, Phys. Rev. B **100**, 195139 (2019).
[18] S.-H. Zhang and W. Yang, New J. Phys. **21**, 103052 (2019).
[19] G. C. Paul, SK Firoz Islam, and A. Saha, Phys. Rev. B **99**, 155418 (2019).
[20] A. E. Champo and G. G. Naumis, Phys. Rev. B **99**, 035415 (2019).
[21] B. D. Napitu, J. Appl. Phys. **127**, 034303 (2020).

[22] R. Bistritzer and A. H. MacDonald, Proc. Natl. Acad. Sci. USA **108**, 12233 (2011).
[23] Y. Cao, V. Fatemi, S. Fang, K. Watanabe, T. Taniguchi, E. Kaxiras, and P. Jarillo-Herrero, Nature (London) **556**, 43 (2018).
[24] Z. Hao, A. M. Zimmerman, P. Ledwith, E. Khalaf, D. H. Najafabadi, K. Watanabe, T. Taniguchi, A. Vishwanath, and P. Kim, Science **371**, 1133 (2021).
[25] A. L. Sharpe, E. J. Fox, A. W. Barnard, J. Finney, K. Watanabe, T. Taniguchi, M. A. Kastner, and D. Goldhaber-Gordon, Science **365**, 605 (2019).
[26] K. P. Nuckolls, M. Oh, D. Wong, B. Lian, K. Watanabe, T. Taniguchi, B. A. Bernevig, and A. Yazdani, Nature (London) **588**, 610 (2020).
[27] H. Weng, Y. Liang, Q. Xu, R. Yu, Z. Fang, X. Dai, and Y. Kawazoe, Phys. Rev. B **92**, 045108 (2015).
[28] J.-T. Wang, H. Weng, S. Nie, Z. Fang, Y. Kawazoe, and C. Chen, Phys. Rev. Lett. **116**, 195501 (2016).
[29] Y. Du, F. Tang, D. Wang, L. Shen, E. Kan, C.-G. Duan, S. Y. Savrasov, and X. Wan, npj Quantum Mater. **2**, 3 (2017).
[30] J. Behrends, J.-W. Rhim, S. Liu, A. G. Grushin, and J. H. Bardarson, Phys. Rev. B **96**, 245101 (2017).
[31] X. Zhang, L. Jin, X. Dai, and G. Liu, J. Phys. Chem. Lett. **8**, 4814 (2017).
[32] P. E. Blöchl, Phys. Rev. B **50**, 17953 (1994).
[33] G. Kresse and J. Furthmüller, Comput. Mater. Sci. **6**, 15 (1996).
[34] J. P. Perdew, K. Burke, and M. Ernzerhof, Phys. Rev. Lett. **77**, 3865 (1996).
[35] S. Grimme, J. Antony, S. Ehrlich, and H. Krieg, J. Chem. Phys. **132**, 154104 (2010).
[36] A. Togo, F. Oba, and I. Tanaka, Phys. Rev. B **78**, 134106 (2008).
[37] R. Car and M. Parrinello, Phys. Rev. Lett. **55**, 2471 (1985).
[38] L. Cui, T. Song, J. Cai, X. Cui, Z. Liu, and J. Zhao, Phys. Rev. B **102**, 155133 (2020).
[39] Y. Gao, Y. Xie, Y. Chen, J. Gu, and Z. Chen, Phys. Chem. Chem. Phys. **20**, 23500 (2018).
[40] H. Tang and S. Ismail-Beigi, Phys. Rev. Lett. **99**, 115501 (2007).
[41] R. W. G. Wyckoff, *Crystal Structures* (Interscience Publishers, New York, 1963), Vol. 1.
[42] X.-L. He, X. Shao, T. Chen, Y.-K. Tai, X.-J. Weng, Q. Chen, X. Dong, G. Gao, J. Sun, X.-F. Zhou, Y. Tian, and H.-T. Wang, Phys. Rev. B **99**, 184111 (2019).
[43] H. Zhong, K. Huang, G. Yu, and S. Yuan, Phys. Rev. B **98**, 054104 (2018).
[44] W. L. Mao, H. Mao, P. J. Eng, T. P. Trainor, M. Newville, C. Kao, D. L. Heinz, J. Shu, Y. Meng, and R. J. Hemley, Science **302**, 425 (2003).
[45] Z. Wang, Y. Zhao, K. Tait, X. Liao, D. Schiferl, C. Zha, R. T. Downs, J. Qian, Y. Zhu, and T. Shen, Proc. Natl. Acad. Sci. USA **101**, 13699 (2004).
[46] See Supplemental Material at http://link.aps.org/supplemental/10.1103/PhysRevB.105.235410 for additional discussion and reference [53] about the electronic structures, molecular dynamics simulations, and topological analysis.
[47] N. B. Kopnin, T. T. Heikkilä, and G. E. Volovik, Phys. Rev. B **83**, 220503 (2011).
[48] T. Bzdušek, Q. Wu, A. Rüegg, M. Sigrist, and A. A. Soluyanov, Nature (London) **538**, 75 (2016).
[49] X. Dong, A. R. Oganov, A. F. Goncharov, E. Stavrou, S. Lobanov, G. Saleh, G.-R. Qian, Q. Zhu, C. Gatti, V. L. Deringer, R. Dronskowski, X.-F. Zhou, V. B. Prakapenka, Z. Konôpková, I. A. Popov, A. I. Boldyrev, and H.-T. Wang, Nat. Chem. **9**, 440 (2017).
[50] X. Liu, Q. Li, Q. Ruan, M. S. Rahn, B. I. Yakobson, and M. C. Hersam, Nat. Mater. **21**, 35 (2022).
[51] C. Chen, H. Lv, P. Zhang, Z. Zhuo, Y. Wang, C. Ma, W. Li, X. Wang, B. Feng, P. Cheng, X. Wu, K. Wu, and L. Chen, Nat. Chem. **14**, 25 (2022).
[52] X.-L. He, X.-J. Weng, Y. Zhang, Z. Zhao, Z. Wang, B. Xu, A. R. Oganov, Y. Tian, X.-F. Zhou, and H.-T. Wang, FlatChem **7**, 34 (2018).
[53] J. Gao, Q. Wu, C. Persson, and Z. Wang, Comput. Phys. Commun. **261**, 107760 (2021).